Original Article

Institution of MECHANICAL ENGINEERS
Journal of MULTI-BODY DYNAMICS

Proc IMechE Part K:
J Multi-body Dynamics
1–17


Article reuse guidelines:
sagepub.com/journals-permissions
DOI: 10.1177/14644193231161136
journals.sagepub.com/home/pik
SAGE

Nonlinear tribodynamics of an elastic shaft with a flexible bearing outer race

Robert Turnbull[1], Nader Dolatabadi[1], Ramin Rahmani[1] and Homer Rahnejat[1,2]

Abstract

In this paper, a mathematical model of a rotor-bearing system is presented. The model includes modal elastodynamics of a flexible rotor as well as the in-plane radial dynamics of the bearing with a flexible outer race. Elastodynamics of the flexible shaft utilises a solution based on Green's function to provide a computationally efficient approach. The flexible bearing outer race is modelled using Timoshenko beam theory. The system model also includes detailed lubricated contact mechanics of balls-to-races contacts with viscous friction. Therefore, the rotor-bearing analysis represents a detailed multi-physics tribodynamics and modal elastodynamic responses of the system which closely represents broad-band vibration response of such systems in practice, an approach not hitherto reported in the literature. It is also demonstrated that the outer race flexibility changes the location of the stability orbital centres, as well as the spread of limit cycle vibrations. Furthermore, it accentuates the occurrence of multiples of ball pass frequency. The importance of integrated system dynamics and lubricated contact mechanics is highlighted, showing that although the elastodynamic response of the rotor's flexible elements may not be clear in the acquired vibration signal, its effect on energy efficiency of the system can be quite important.

Keywords

rotordynamics, vibration of ball bearings, elastodynamics, flexible bearing race, lubricated contact dynamics

Date received: 27 October 2022; accepted: 15 February 2023

Introduction

Bearing supports are often the limiting factor for the performance of any machine and mechanism which they are a part. The key issues of concern with bearings are thermal stability,[1–3] wear and fatigue of rolling mating surfaces,[4–8] and noise and vibration.[9–12] During operation, the rolling elements within a bearing undergo complex motions such as rolling and sliding relative to the raceway grooves, as well as convergence and separation of the bearing rings.[13] Therefore, use of a bearing dynamics model is a prerequisite to any investigation of its performance, such as reliability, structural integrity, fatigue, wear, and operational efficiency.

Sunnersjö[14] was one of the first to investigate the effect of applied inertial forces using a two degree-of-freedom (2 DOF) bearing dynamics model. Rahnejat and Gohar[15] improved on the work of Sunnersjö[14] by including lubricated balls-to-races contacts under various regimes of lubrication. This was further extended by Aini et al.[16] in a 5 DOF ball-bearing model including radial, thrust, and moment loading. For rolling element bearings, the effect of roller tilting, yawing, and squeeze film motions as well as lubricated contacts have been taken into account by various researchers.[17–20]

Additionally, the lubricated contact of rolling elements to races in bearings is often subjected to high shear, resulting in generated heat and lubricant non-Newtonian traction. Mohammadpour et al.[21] extended the previous lubricated contact dynamics analysis of Aini et al.[16] to include these effects in their bearing dynamics analysis model. A recent detailed thermal model was also presented by Alfares et al.[22]

Another salient practical feature for modelling of shaft and bearing systems is the flexibility of bearing rings or the bearing housing which influences the dynamic performance of shaft and bearing systems.[23–27] The flexibility of the rotor itself also affects the rotor-bearing system dynamics.[28–31] In fact, there are a host of practical features which may be incorporated in bearing dynamic analysis. Consequently, there has been a plethora of research in the area of rolling element dynamics, with most focusing on certain specific aspects.

This paper presents a 2 DOF bearing dynamics model, which integrates the transient elastodynamic response of

[1]Wolfson School of Mechanical, Electrical and Manufacturing Engineering, Loughborough University, Loughborough, UK
[2]School of Engineering, University of Central Lancashire, Preston, UK

Corresponding author:
Ramin Rahmani, Wolfson School of Mechanical, Electrical and Manufacturing Engineering, Loughborough University, Loughborough, UK.
Email: r.rahmani@lboro.ac.uk

the bearing's flexible outer race with elastohydrodynamics of balls-to-races contacts. In this manner, both the localised Hertzian deflection and global elastic deformation of the bearing's outer ring are taken into account. The outer race of the bearing is considered an elastic thick complete circular ring, because in practice the radius-to-width ratio of the outer ring is less than 10 and according to Chidamparam and Leissa[32] this requires the use of a Timoshenko beam model. Therefore, elastodynamics of the flexible ring is based on Timoshenko (or Timoshenko–Ehrenfest) thick ring theory,[33] thus including the effect of rotational bending and shear deformation. The numerical solution of full-bearing dynamics with a flexible ring is quite time-consuming. Consequently, an analytical model for the elastodynamic response of the shaft is developed, which is based upon Green's function approach. Therefore, realistic elastodynamics of a flexible rotor-bearing system with non-Newtonian piezo-viscous lubricated contacts is presented, an approach not hitherto reported in the literature.

Model description

Rotor-bearing model

Figure 1(a) is a schematic representation of an elastic rotor supported by a pair of deep groove ball bearings. Figure 1(b) shows a deep groove ball bearing, where the instantaneous dynamic load carried by the ball complement is determined by the lateral excursions of the shaft centre from that of the support bearings in the transversal radial x and y directions.

For the 2 DOF bearing dynamics model the following assumptions are made:

1. The inner and outer bearing races are considered to be perfectly circular.
2. The balls are considered to be perfectly spherical and have identical diameters (i.e., there are no off-sized rolling elements).
3. The balls are considered to be massless compared with the supported shaft and bearing rings and remain equi-pitched around the bearings.
4. Bearings are subjected to radial transverse loading only.
5. Thermal effects are neglected (these will affect dimensional stability, interference fitting and preloading of the bearing,[1–3] as well as lubricant rheology in the contact).[34]

These assumptions lead to a 2 DOF bearing model described in the study by Rahnejat and Gohar[15,35] for a radial deep groove ball bearing. The equations of motion become:

$$M\ddot{x} = \sum_{i=1}^{m}(-W_i\cos\theta_i) - Mg + F_x \tag{1}$$

$$M\ddot{y} = \sum_{i=1}^{m}(-W_i\sin\theta_i) + F_y \tag{2}$$

where F_x and F_y are any externally applied forces in the x and y directions, respectively. M denotes the shaft mass, θ_i is the instantaneous circumferential angular position of the i-th ball around the raceway, and W_i is the corresponding instantaneous contact load, acting radially towards the centre of the bearing. The balls-to-races contact reactions are determined by the Hertzian contact theory as:

$$W_i = K\delta_i^{n'} \tag{3}$$

where K is the contact stiffness nonlinearity, δ_i is the localised Hertzian contact deflection for the i-th ball, and W_i is the corresponding contact reaction. The exponent n' is 1.5 for a ball bearing and 1.11 for a cylindrical rolling element bearing.[7,35]

The localised contact deflection of the i-th ball, δ_i, is obtained as[15,35]:

$$2\delta_i = 2(h_i - C) + x\cos\theta_i + y\sin\theta_i \tag{4}$$

where x and y are the movements of the bearing centre corresponding to the instantaneous circumferential orbital position of the i-th ball, θ_i. C is the radial clearance and h_i is the lubricant film thickness. The deflection is further modified including the effect of the flexible outer ring's global radial deflection at any contact location, u_i[25]:

$$2\delta_i = 2(h_i - C) + x\cos\theta_i + y\sin\theta_i + u_i \tag{5}$$

The combined contact stiffness nonlinearity, K, of any of the ball-to-inner and ball-to-outer races contacts are determined as[36,37]:

$$K_l = \sqrt{\frac{e}{\lambda_l^3}\kappa_C},\ l \in \{1, 2\} \tag{6}$$

where 1 denotes the contact with the inner race and 2 for the outer race. κ_C is the elastic proportionality constant[36]:

$$\kappa_C = \frac{8}{3}\frac{E_1E_2}{E_1(1-\nu_2^2) + E_2(1-\nu_1^2)} \tag{7}$$

where E and ν are Young's modulus of elasticity and Poisson's ratio for contacting bodies. In addition, the curvature sum for the ball-to-the inner and ball-to-outer raceways is[37]:

$$e = \frac{4}{R_1^{-1} + R_1'^{-1} + R_2^{-1} + R_2'^{-1}} \tag{8}$$

where R_1 and R_2 are the radii of curvature of the rolling element in the zx and zy planes of contact (z denotes the direction of the contact normal). Clearly, for a ball bearing $R_1 = R_2$, and the radii of curvature of the inner and outer raceways are R_1' and R_2', respectively. λ is the contact footprint ellipticity ratio and α and β are

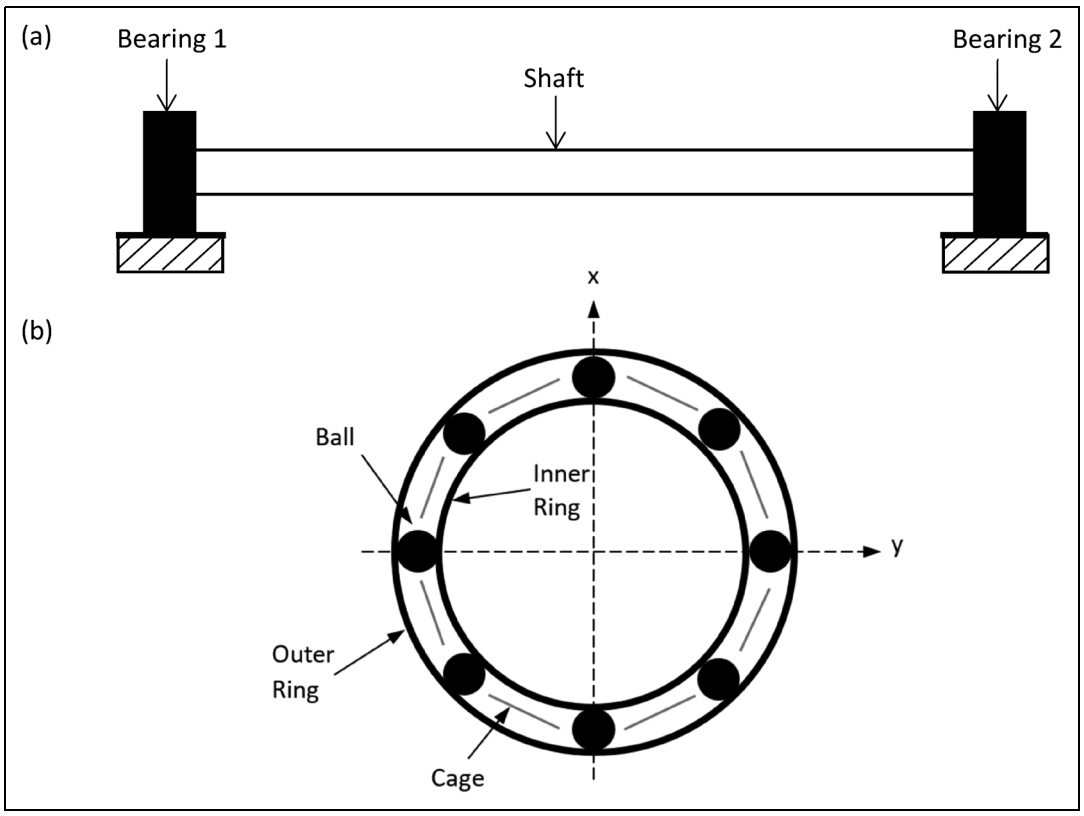

Figure 1. (a) Overview of rotor system, (b) 2 degree-of-freedom deep groove ball bearing dynamic model.

transcendental functions of the angle ψ, all of which are provided in Table 1[25,36]:

$$\psi = \cos^{-1}\left[-\frac{e}{4}\sqrt{\left(\frac{1}{R_1}-\frac{1}{R_1'}\right)^2+\left(\frac{1}{R_2}-\frac{1}{R_2'}\right)^2+2\left(\frac{1}{R_1}-\frac{1}{R_1'}\right)\left(\frac{1}{R_2}-\frac{1}{R_2'}\right)\cos 2\phi}\right] \tag{9}$$

The effective contact stiffness for a ball-to-races contacts becomes:

$$K = \left(\frac{1}{K_1^{-2/3}+K_2^{-2/3}}\right)^{3/2} \tag{10}$$

The maximum Hertzian contact pressure for the i-th contact becomes[38]:

$$p_{0i} = \frac{3W_i}{2\pi a_i b_i} \tag{11}$$

where the semi-major and semi-minor half-widths for the elliptical point contact footprint are, respectively:

$$a_i = \alpha\left(\frac{W_i e}{\kappa_C}\right)^{\frac{1}{3}} \tag{12}$$

$$b_i = \beta\left(\frac{W_i e}{\kappa_C}\right)^{\frac{1}{3}} \tag{13}$$

To determine the film thickness for lubricated contacts of the balls to raceway grooves one can use an extrapolated oil film thickness equation as initially shown in Rahnejat and Gohar.[15] These expressions are obtained by regression of many numerically predicted results based on the variation of a number of dimensionless parameters which represent a broad range of representative operating conditions in contacts subject to EHL. In the current study, the expression obtained by Hamrock and Dowson[39] is used:

$$H_{ci}^{*}=2.69U^{*0.67}G^{*0.53}W^{*-0.067}[1-\exp(-0.73\lambda)] \tag{14}$$

Table 1. Contact mechanics parameters.[25,34,35]

ψ	0°	10°	20°	30°	35°	40°	45°	50°	55°	60°	65°	70°	75°	80°	85°	90°
α	∞	6.612	3.778	2.731	2.397	2.136	1.926	1.754	1.611	1.486	1.387	1.284	1.202	1.128	1.061	1.00
β	0	0.319	0.408	0.493	0.530	0.567	0.604	0.641	0.678	0.717	0.759	0.802	0.846	0.893	0.944	1.00
λ	-	0.851	1.220	1.453	1.550	1.637	1.709	1.772	1.828	1.875	1.912	1.944	1.967	1.985	1.996	2.00

where H_{ci}^* is the dimensionless central contact lubricant film thickness:

$$H_{ci}^* = \frac{h_i}{R_x} \tag{15}$$

in which: $R_x^{-1} = R_1^{-1} + R_1'^{-1}$.

The dimensionless parameters in equation (14) are:

$$U^* = \frac{\eta_0 U}{E' R_x},\ W_i^* = \frac{W_i}{E' R_x^2},\ G^* = \alpha_p E',\ \lambda = \frac{a_i}{b_i} \tag{16}$$

where η_0 is the lubricant dynamic viscosity, U is the velocity of lubricant entrainment into the contact, α_p is the lubricant piezo-viscosity coefficient, and λ is the ellipticity ratio. The reduced plane strain modulus of elasticity of the contacting pair, both made of the same material (cobalt-chromium bearing steel), is: $E' = E / (1 - \nu^2)$.

Having obtained the lubricant film thickness for all the balls-to-races contacts, the viscous shear stress in all contacts can be obtained as Gohar and Rahnejat[38]:

$$\tau_i = \frac{\eta_i \Delta u}{h_i} \tag{17}$$

where for the assumed isothermal solution in the current analysis the effective lubricant viscosity in the i-th ball's contact is adjusted for the mean contact pressure, p_m using Roelands[40]:

$$\eta_i = \eta_0 \exp\left\{ \ln\left(\frac{\eta_0}{\eta_r}\right)\left[\left(1 + \frac{p_{mi}}{p_r}\right)^{Z_0} - 1 \right] \right\} \tag{18}$$

where for the i-th contact the mean contact pressure is:

$$p_{mi} = \frac{2}{3} p_{0i} \tag{19}$$

Friction is mainly generated by sliding in the contact, promoting viscous shear of the lubricant. The sliding velocity Δu in equation (17) is the relative speed of the balls to the races as the rolling elements roll and slide relative to the races due to the existence of a curvilinear ellipse in space.[41] As the balls remain equi-pitched, the sliding velocity for all contacts is assumed to be the same, ignoring any microslip conditions. For a deep groove radial ball bearing, the sliding velocity is[41]:

$$\Delta u = \frac{u_s}{2}\left(1 + \frac{R}{R_1'}\right) \tag{20}$$

where u_s is the surface speed of the inner race, assumed to be the same as that of the rotor surface.

The shear stress in equation (17) is under Newtonian shear of the lubricant. With increased contact load and contact sliding, the lubricant traction may exceed the Eyring shear stress,[42] where the lubricant behaviour is termed non-Newtonian. Thus[43]:

$$\tau_i = \tau_0 + \varepsilon p_m \tag{21}$$

where ε is the slope of the lubricant limiting shear stress with changes in pressure. This may be obtained for a lubricant through traction measurement procedures using, for example, a disc machine. In the current study: $\varepsilon = 0.08$.

Assuming smooth contacting surfaces, friction is mainly generated by the viscous shear of the lubricant. Thus, for the i-th elliptical point contact[38]:

$$F_{fi} = \pi a_i b_i \tau_i \tag{22}$$

and the associated instantaneous power loss becomes:

$$P_{li} = F_{fi} \frac{R_{io}}{f_{sh}} \tag{23}$$

where f_{sh} is the shaft rotational frequency and R_{io} is the inside radius of the outer race.

The total bearing power loss is:

$$P = \sum_i P_{li} \tag{24}$$

Elastodynamics of the rotor

The flexibility of the supported rotor is included in the 2 DOF system dynamics model. It is assumed that the shaft is free at both ends and subjected to excitation forces at the bearing supports. The equation of motion for such an elastic shaft is given as:

$$\rho A \frac{\partial^2 u_e(z,t)}{\partial t^2} + EI \frac{\partial^4 u_e(z,t)}{\partial z^4} = f_e(z,t) \tag{25}$$

where u_e is the local lateral shaft deflection, $z \in [0, l]$ is the position along the shaft, t is time, f_e is the applied excitation force per unit shaft length, E is Young's modulus of elasticity, ρ is the shaft material density, I is the second moment of area of the shaft cross-section with respect to the lateral axis, and A_s is the cross-sectional area of the shaft. The analytical closed-form solution for the shaft vibration is given as[44]:

$$\begin{aligned} u_e(z,t) = {} & \frac{\partial}{\partial t}\int_0^l f_0(\xi) G(z,\xi,t) d\xi \\ & + \int_0^l g_0(\xi) G(z,\xi,t) d\xi \\ & + \int_0^t \int_0^l a_e(\xi,\zeta) G(z,\xi,t-\tau) d\xi d\zeta \end{aligned} \tag{26}$$

where f_0 and g_0 are the initial conditions in terms of deflection and velocity profiles of the shaft, and $a_e = f_e / (\rho A)$ is the excitation acceleration. For a shaft with free-free boundary conditions, where:

$$\frac{\partial^2 u_e}{\partial z^2}(0, t) = \frac{\partial^3 u_e}{\partial z^3}(0, t) = \frac{\partial^2 u_e}{\partial z^2}(l, t) = \frac{\partial^3 u_e}{\partial z^3}(l, t) = 0 \tag{27}$$

the Green's function becomes:

$$G(z, \xi, t) = \frac{t}{l} + \frac{3t}{l^3}(2z - l)(2\xi - l) + \frac{4}{cl}\sum_{n=1}^{\infty} \frac{\varphi_n(z)\varphi_n(\xi)}{\lambda_n^2 \varphi_n^2(l)} \sin(\lambda_n^2 ct) \tag{28}$$

where $c = \sqrt{EI / \rho A}$ and:

$$\varphi_n(z) = (\sinh \lambda_n l - \sin \lambda_n l)(\cosh \lambda_n z + \cos \lambda_n z) - (\cosh \lambda_n l - \cos \lambda_n l)(\sinh \lambda_n z + \sin \lambda_n z) \tag{29}$$

in which, $\lambda_n = \psi_n / l$, where $\psi_1 = 1.875$, $\psi_2 = 4.694$, and for $n \geq 3$, $\psi_n = \pi(2n - 1) / 2$.

One of the advantages of using this approach over the conventional modal analysis method is that it simultaneously provides the natural frequencies and mode shapes. Note that the first two terms in the expression for the Green's function are associated with the zero eigenvalue with two orthogonal functions 1 and $(2z - l)$.

The applied force for the rotor shown in Figure 1 has the following general piecewise profile:

$$f_e(z, t) = \begin{cases} 0 & z \in [0, l_1) \\ f_1(t) & z = l_1 \\ 0 & z \in (l_1, l_2) \\ f_2(t) & z = l_2 \\ 0 & z \in (l_2, l] \end{cases} \tag{30}$$

where $f_1(t)$is the reaction of bearing 1 at position $z = l_1$, $f_2(t)$is that for bearing 2 at position $z = l_2$, and $l$is the length of the shaft. The advantage of using Green's function approach is that it allows the inclusion of a wide range of loading conditions, such as unbalanced forces. This is because it provides a closed-form solution for a flexible shaft subjected to a generalised force profile. Assuming that the bearings are located at both ends of the shaft, the final solution for the shaft vibration becomes:

$$\begin{aligned} u_e(z, t) = {} & f_0 \left\{ 1 + \frac{4}{l}\sum_{n=1}^{\infty} \frac{\varphi_n(z)\cos(\lambda_n^2 a_e t)}{\lambda_n \varphi_n^2(l)} [(\sinh \lambda_n l - \sin \lambda_n l)^2 - (\cosh \lambda_n l - \cos \lambda_n l)^2] \right\} \\ & + g_0 \left\{ t + \frac{4}{a_e l}\sum_{n=1}^{\infty} \frac{\varphi_n(z)\sin(\lambda_n^2 a_e t)}{\lambda_n^3 \varphi_n^2(l)} [(\sinh^2 \lambda_n l - \sin^2 \lambda_n l) - (\cosh \lambda_n l - \cos \lambda_n l)^2] \right\} \\ & + \int_0^t \int_0^l [f_1(t)\delta_d(\xi - l_1) + f_2(t)\delta_d(\xi - l_2) + f_3(t)\delta_d(\xi - l_3)] \\ & \times \left\{ \frac{t}{l} + \frac{3t}{l^3}(2z - l)(2\xi - l) + \frac{4}{a_e l}\sum_{n=1}^{\infty} \frac{\varphi_n(z)\varphi_n(\xi)}{\lambda_n^2 \varphi_n^2(l)} \sin(\lambda_n^2 a_e (t - \zeta)) \right\} d\xi d\zeta \end{aligned} \tag{31}$$

where δ_d is the Dirac delta function and ξ and ζ are intermediate spatial and temporal integration variables. Equation (31) is obtained from equation (26) by replacing Green's function from equation (28) and performing the differentiation and integration associated with the initial conditions (i.e., the terms that include f_0 and g_0). In addition, since the load is applied at specific points along the shaft, the Dirac delta function has been used to introduce the load in the solution. This allows for switching the load terms when the integration process involves a desired point.

In-plane elastodynamics of the bearing outer race

The global modal deflection of an outer flexible bearing ring is included in the 2 DOF bearing dynamics model (i.e., u_i in equation (5)). The outer bearing ring is considered a thick complete circular elastic ring. An in-depth

study of a bearing race as a thick ring and its integration with the bearing dynamics is shown in Kerst et al.[25] In this study the approach for a single ball bearing demonstrated in Kerst et al.[25] is expanded for a rotor system that includes two ball bearings separated by a flexible shaft. Each of the ball bearings are modelled to include the in-plane vibrations within the 2 DOF bearing dynamics.

The coupled in-plane equations of motion for a thick ring segment representing the outer race of a ball bearing, including shearing deformation and rotary inertia are obtained as[45]:

$$\frac{\kappa_s A_o G_s}{R_o}\left(\frac{\partial^2 u}{\partial\theta^2}+\frac{\partial w}{\partial\theta}-R_o\frac{\partial\phi}{\partial\theta}\right)+\frac{EA_o}{R_o}\left(\frac{\partial w}{\partial\theta}-u\right)+f_r R_o=\rho_o A_o R_o\frac{\partial^2 u}{\partial t^2} \tag{32}$$

$$\frac{EA_o}{R_o}\left(\frac{\partial^2 w}{\partial\theta^2}-\frac{\partial u}{\partial\theta}\right)-\frac{\kappa_s A_o G_s}{R_o}\left(\frac{\partial u}{\partial\theta}+w-R_o\phi\right)+p_c R_o=\rho_o A_o R_o\frac{\partial^2 w}{\partial t^2} \tag{33}$$

$$\frac{EI_1}{R_o}\frac{\partial^2\phi}{\partial\theta^2}+\kappa_s A_o G_s\left(\frac{\partial u}{\partial\theta}+w-R_o\phi\right)=\rho_o I_1 R_o\frac{\partial^2\phi}{\partial t^2} \tag{34}$$

where A_o is the cross-sectional area of the thick outer bearing ring, R_o is its nominal radius, I_1 is the second area moment of inertia of the ring's cross-section, E is the Young's modulus of elasticity of the ring's material, G_s is the shear modulus, ρ_o is the material density, κ_s is the shear correction factor, f_r is the applied radial force, and p_c is the force applied circumferentially. The instantaneous radial global ring deflection is u, and w is its circumferential deflection. The global ring deflection is input into equation (5). Details of the numerical solution of the governing elastodynamic equations for the elastic beam using a finite difference method (FDM) is outlined in the Appendix.

Method of solution

Two multi-physics models are utilised in the current analysis. The first model (the rigid bearing ring model) includes a 2 DOF bearing dynamics model with a flexible rotor. This model assumes that the bearing races are rigid. The second model (the flexible ring dynamics model) removes the assumption of a rigid outer raceway by including the elastodynamics of a flexible outer race. The solution procedure is depicted by the flowchart of Figure 2.

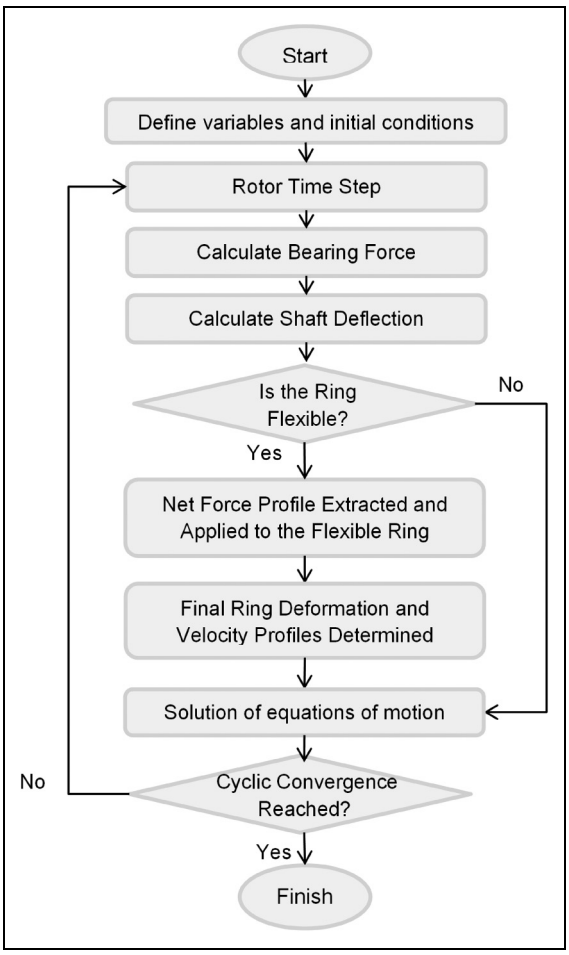

Figure 2. Solution procedure.

Results and discussion

Rotor model validation

The specifications of the rotor-bearing system are listed in Table 2. All the balls-to-race contacts are assumed to remain in compression throughout the balls' orbital motion, thus guarding against a number of undesired phenomena such as ball skewing, rattling and balls-cage collisions. The radii of curvature of the raceway grooves provide a contact conformity of 7% and an angle of 45° using the relations provided in Model description section. The number of balls for a moderately packed arrangement is $Z = 12$.

The component-level predicted response frequencies for the flexible shaft and the flexible bearing outer raceway are first obtained prior to the determination of system level (i.e., the rotor dynamics) analysis. The predicted frequencies for the flexible shaft are compared with the analytical flexible vibration frequencies given by Rao[45] as:

$$\omega=(\beta' l)^2\sqrt{\frac{EI}{\rho A_s l^4}} \tag{35}$$

where $\beta' l$ values are 4.6940, 7.8540, 10.9956, and 14.1372 for the first four flexible modes as indicated in equation (29) (see Table 3).

Table 2. Rotor-bearing system specifications.

Parameter	Value	Unit
Bore	40	mm
Inner race diameter	50	mm
Pitch diameter	56.3	mm
Outer race inner diameter	75.4	mm
Outer race outside diameter	83.7	mm
Width	23.4	mm
Radial clearance	5	mm
Young's modulus of bearing material	210	GPa
Poisson's ratio of bearing material	0.3	-
Number of rollers	12	-
Ball diameter	12.7	mm
K	13.509	GN / $m^{1.5}$
Shaft length	140	mm
Shaft diameter	40	mm
Shaft mass	140	kg
Lubricant dynamic viscosity at 60°C	0.08	Pa.s
Piezo-viscosity coefficient at 60°C	1.44 x10^{-8}	Pa^{-1}

Table 3. Shaft modal response frequencies below 90 kHz.

Mode	Results from[45] (Hz)	Current shaft Model (Hz)	Error (%)
2	9326	9297	−0.31
3	25907	25936	0.11
4	50778	50799	0.04
5	83939	83989	0.06

Table 4. Flexible bearing outer ring modal frequencies below 90 kHz.

Mode	Results from[45] (Hz)	Current ring model (Hz)	Error (%)
2	3626	3671	1.24
3	9899	9867	−0.32
4	18144	18023	−0.67
5	27876	27656	−0.79
6	38710	38382	−0.85
7	50347	49901	−0.89
8	62564	61987	−0.92
9	75197	74472	−0.96
10	88125	87229	−1.02

For a thick flexible ring, the vibration frequencies are given by Rao[45] as:

$$\begin{aligned} &K_2^2(-n^2S_2^2S_1 - S_2^2S_1) \\ &\quad + K_2(n^4S_2 + n^4S_2S_1 - 2S_2n^2 + n^2S_2S_1 + n^2 + S_2 + 1) \\ &\quad + (-n^6 + 2n^4 - n^2) \\ &\quad = 0 \end{aligned} \tag{36}$$

where

$$K_2 = \frac{\rho AR^4}{EI_1}\omega^2, \quad S_1 = \frac{E}{\kappa G}, \; S_2 = \frac{I_1}{AR^2} \tag{37}$$

Table 5. Flexible rotor frequency response compared with Matsubara et al.[28]

Mode	Matsubara et al.[28] (Hz)	Current analysis (Hz)	Error (%)
1	1300	1376	5.85
2	9800	9220	−5.92
3	(-)	25871	(-)
4	50500	50839	0.67

The predicted numerical results are compared with their analytical counterparts in Table 4.

The results obtained for both the flexible shaft (Table 3) and the flexible bearing outer ring dynamics (Table 4) show excellent agreement with the calculated analytical frequencies in Rao.[45]

The next stage in model validation is comparison with the numerical work of Matsubara et al.[28] In this case, the rotor system comprises a flexible shaft, bearing supports, and a rigid outer raceway, subjected to a sinusoidal load of 60 N magnitude at its ends. The resonant frequencies of the rotor are presented alongside the predictions provided by Matsubara et al.[28] Good agreement is found between the predictions of the current model with those in Matsubara et al.[28] as shown in Table 5. It is noted that the model proposed by Matsubara et al.[28] utilised a piece-wise linear approximation of the ball-race contact spring non-linearity in the bearing. In the current model the need for a piece-wise linear approximation has been eliminated. Therefore, the current model predicts frequencies that are similar to the model presented by Matsubara et al.[28] with differences predominantly caused by the piece-wise linear approximation in Matsubara et al.[28]

Nonlinear effects induced by a flexible outer ring

Simulations are carried out at a constant rotational frequency of 13.3 Hz (cage frequency). The dynamic responses of the rotor are compared for the rigid ring and flexible ring models of the bearings. To identify the impact of ring flexibility on rotor dynamics, the system responses are investigated using time histories, phase-plane diagrams, and Fast Fourier Transformation (FFT). Figure 3(a) and (b) shows the variations in the shaft displacements with rigid and flexible bearing outer rings in the vertical, *x*- and horizontal transverse *y*-directions, respectively. Ring flexibility mainly affects the displacements in the *x*-direction (Figure 3(a)). The slower oscillations follow the shaft rotational frequency in both directions. A protuberance appears near the minimum response amplitude in the *x*-direction for both cases due to the interactions of the rolling elements with the flexible ring and shaft. The fast oscillations of the shaft undergo noticeably larger amplitudes in the vicinity of this protuberance, indicating greater interactions between the flexible ring and shaft responses in this region. In the *y*-direction (Figure 3(b)), the amplitude of the rapid oscillations is rather negligible in comparison to that of slow oscillations.

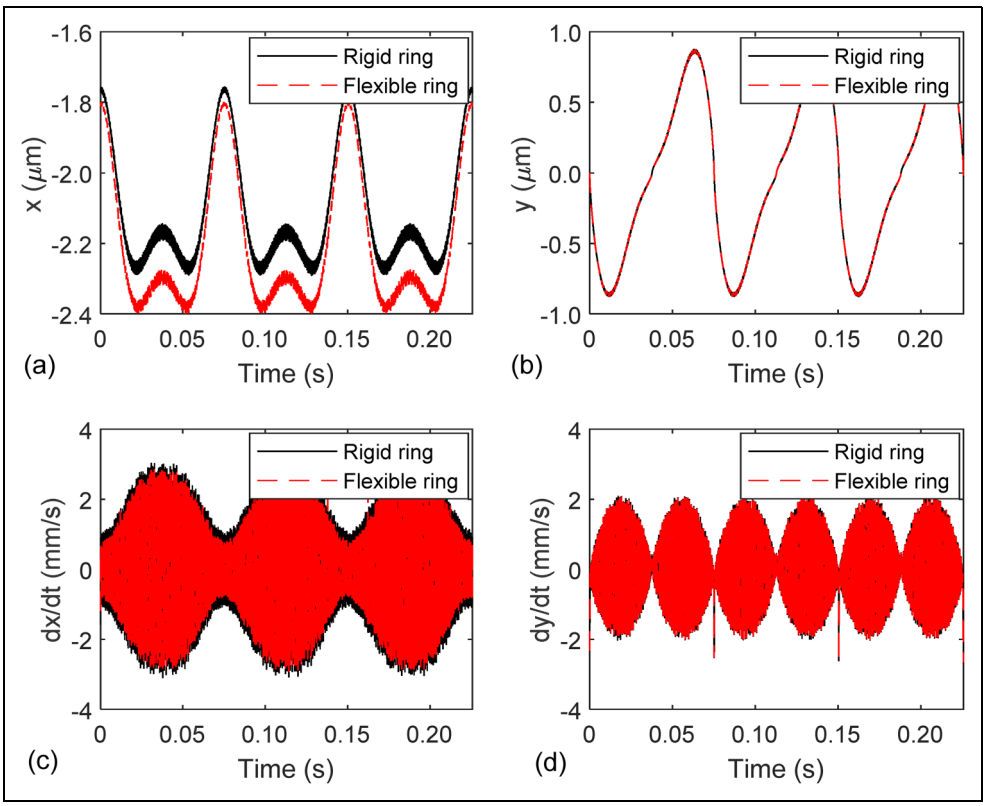

Figure 3. Comparison of shaft vibration time histories for a rigid and a flexible bearing outer ring model: (a) vertical displacement, *x*, (b) horizontal displacement, *y*, (c) vertical velocity, d*x*/d*t*, and (d) horizontal velocity, d*y*/d*t*.

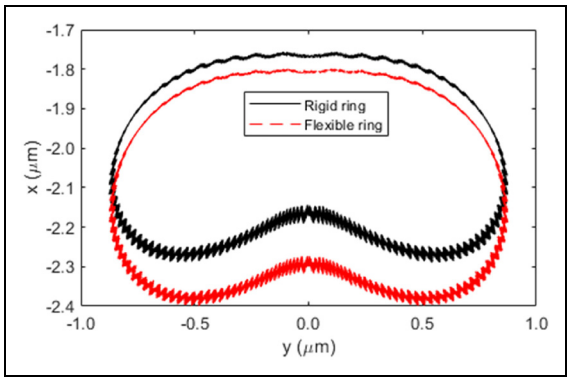

Figure 4. *x*–*y* displacement diagram of shaft centre with rigid and flexible bearing rings models.

The variations in the shaft velocity are largely influenced by the fast oscillations in both directions (Figure 3(c) and (d)). The velocity for the case of an assumed rigid ring shows marginally larger variations in the *x*-direction. The lower velocities for the case of a flexible ring are due to a small increase in the amplitude of displacements of the shaft, which has a larger excursion at the same rotational frequency. The fast variations of the velocity amplitudes in the *x*-direction are constrained by a slow frequency envelope related to the shaft rotation. The envelope wave in the *y*-direction fluctuates at twice the shaft rotational frequency (Figure 3(d)). A spike appears at around 0.075 s when the shaft undergoes maximum displacement in the *x*-direction (Figure 3(d)). At this position, the interference between the shaft and rolling elements reduces and the rolling elements-to-races contact loads attain their minimum value. Hence, the spike can be related to a sudden transition of the shaft over the rolling element bearings. In the *y*-direction, the rigid and flexible ring models are largely identical due to the fact that the shaft is unloaded in this direction.

The transverse *x*-*y* displacement plot of the bearing centre with and without a flexible outer ring is shown in Figure 4. The results in this figure show a slight increase in the amplitude of vibrations for the flexible bearing outer ring. This is due to the deflection of the flexible ring, causing waviness of its surface, affecting the contact of the ball complement in their orbital motion. In turn, this increases vibration of the shaft centre as an excursion from the geometric centre of its bearing support.

The stability of the shaft vibrations is studied through phase-plane diagrams. The cloud representation of the phase-displacement diagram is shown for the shaft vibrations using the assumed rigid bearing outer ring model (Figure 5). The shaft is located at the maximum and minimum amplitudes in the *x* direction in the regions (A) and (C), respectively (Figure 5(a)). Region (B) shows the shaft transitions between the regions (A) and (C). The phase-displacement diagram shows multiple limit cycle trajectories (cloud cyclone). The behaviour of these trajectories conforms to the findings in the time histories of shaft vibrations. Centre of each limit cycle

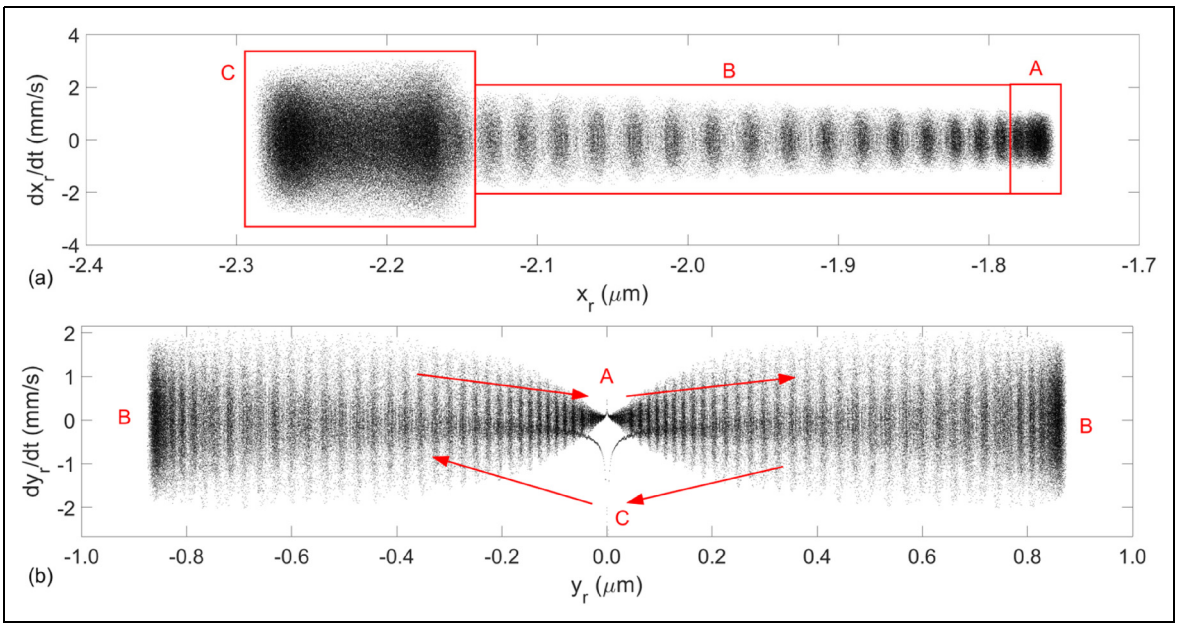

Figure 5. Phase-displacement cloud diagrams of shaft vibrations with rigid ring: (a) vertical components, dx_r/dt-x_r, (b) horizontal components, dy_r/dt-y_r.

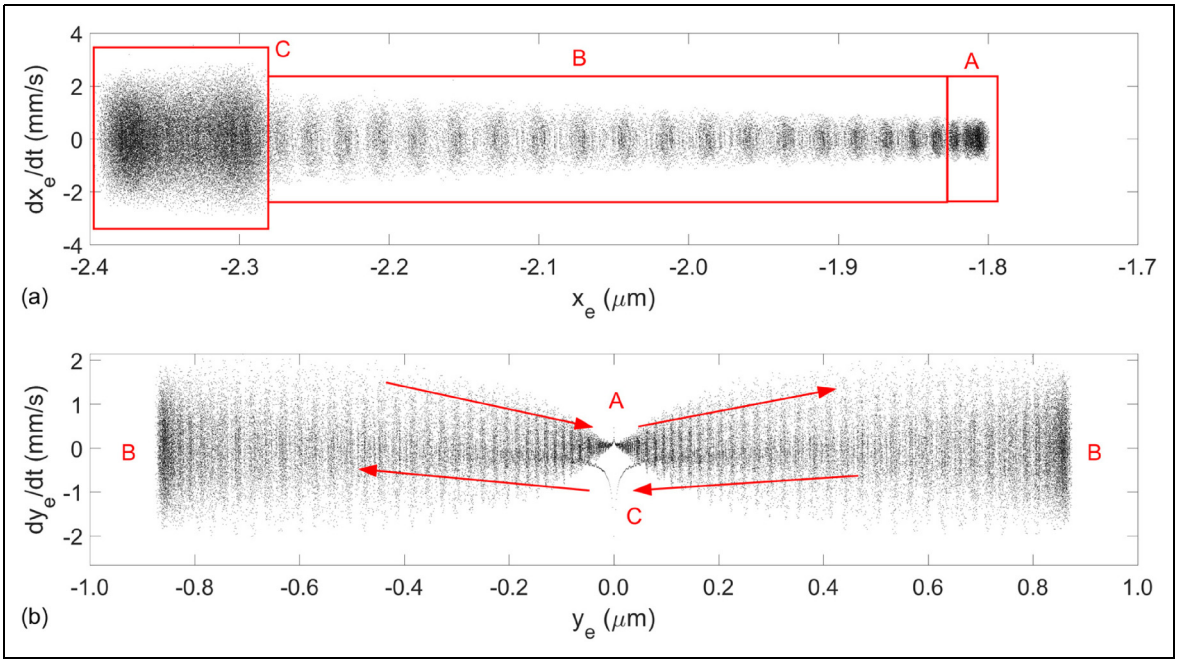

Figure 6. Phase-displacement cloud diagrams of shaft vibrations with flexible ring: (a) vertical components, dx_e/dt-x_e, (b) horizontal components, dy_e/dt-y_e.

represents the point of stability with respect to the centre of the shaft cross-section at each position. The limit cycles about these centres are associated with the flexible shaft vibrations. These centres, however, displace with the rigid body motion of the shaft. Hence, the limit cycles are spread in the x-direction. The shaft has a minimum energy level in the region (A). Therefore, the cloud limit cycle shows a smaller spread/domain. In region (C), the flexible shaft vibrations and their interaction with the orbital motion of the rolling elements are significant, increasing the excitation energy. Hence, the limit cycles fluctuate with a larger spread. This behaviour indicates that the shaft is less stable when it modulates with the motion of the rolling elements. The limit cycle near $x_r = -2.18\ \mu m$ is associated with the protuberance signature in the time history. The limit cycles merge in this region due to an increase in the amplitude contribution from the higher frequency vibrations. During the transition in region (B), these limit cycles are distinctively spaced at regular intervals. Similar trends can be observed in the y-direction oscillations (Figure 5(b)). At the maximum x position (region (A)), the shaft is largely stable in the

y-direction. A sudden spike disturbs the shaft during transition through the neutral position: $y_r = 0$. The vibrations in the y-direction are less stable between regions (A) and (B). As the shaft displaces toward the minimum x position (reversal at region (B) toward region (C)), the size of the limit cycles reduces rapidly in the y-direction. However, a larger excitation immediately disturbs the shaft near $y_r = 0$. This behaviour is symmetric about $y_r = 0$ and seems to be due to a greater interaction/modulation effect between shaft and bearing rolling elements. Such phenomena observed in practice are often referred to as chaotic vibration of bearing supports and are often associated with some loss of preload or changes in interference fit. In the y-direction, the shaft has a generic stability around $y_r = 0$ and the local stability points during the transition of the limit cycles.

Figure 6 shows the phase-plane diagrams for the flexible bearing outer ring model. The behaviour of the shaft in this flexible model is largely similar to that of an assumed rigid shaft. In the x-direction, the transition regions are stretched, indicating larger displacements. The limits of regions (A) and (C) are also displaced to

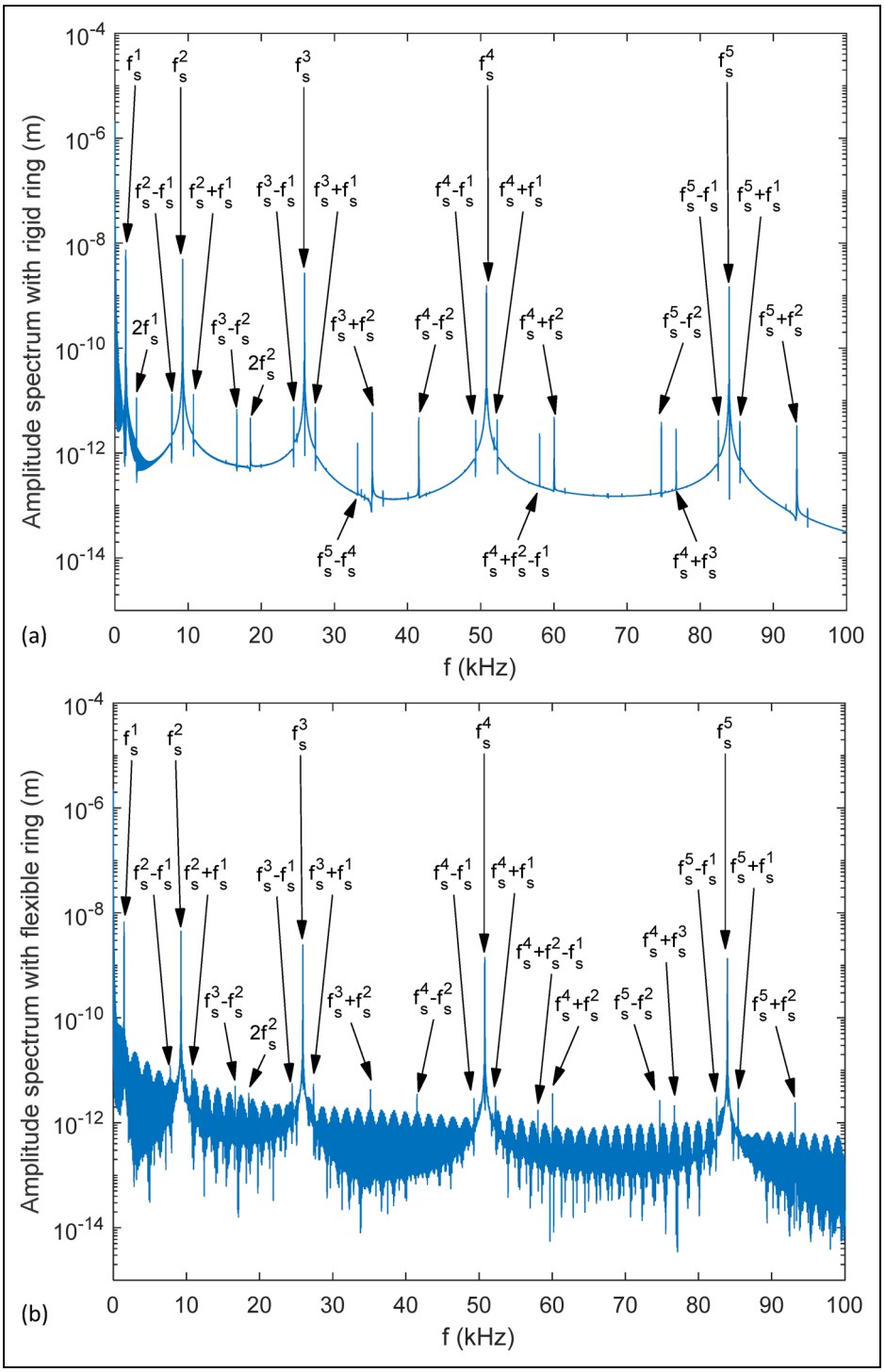

Figure 7. Spectrum of shaft vibrations in the band: 0–100 kHz: (a) rigid ring and (b) flexible ring.

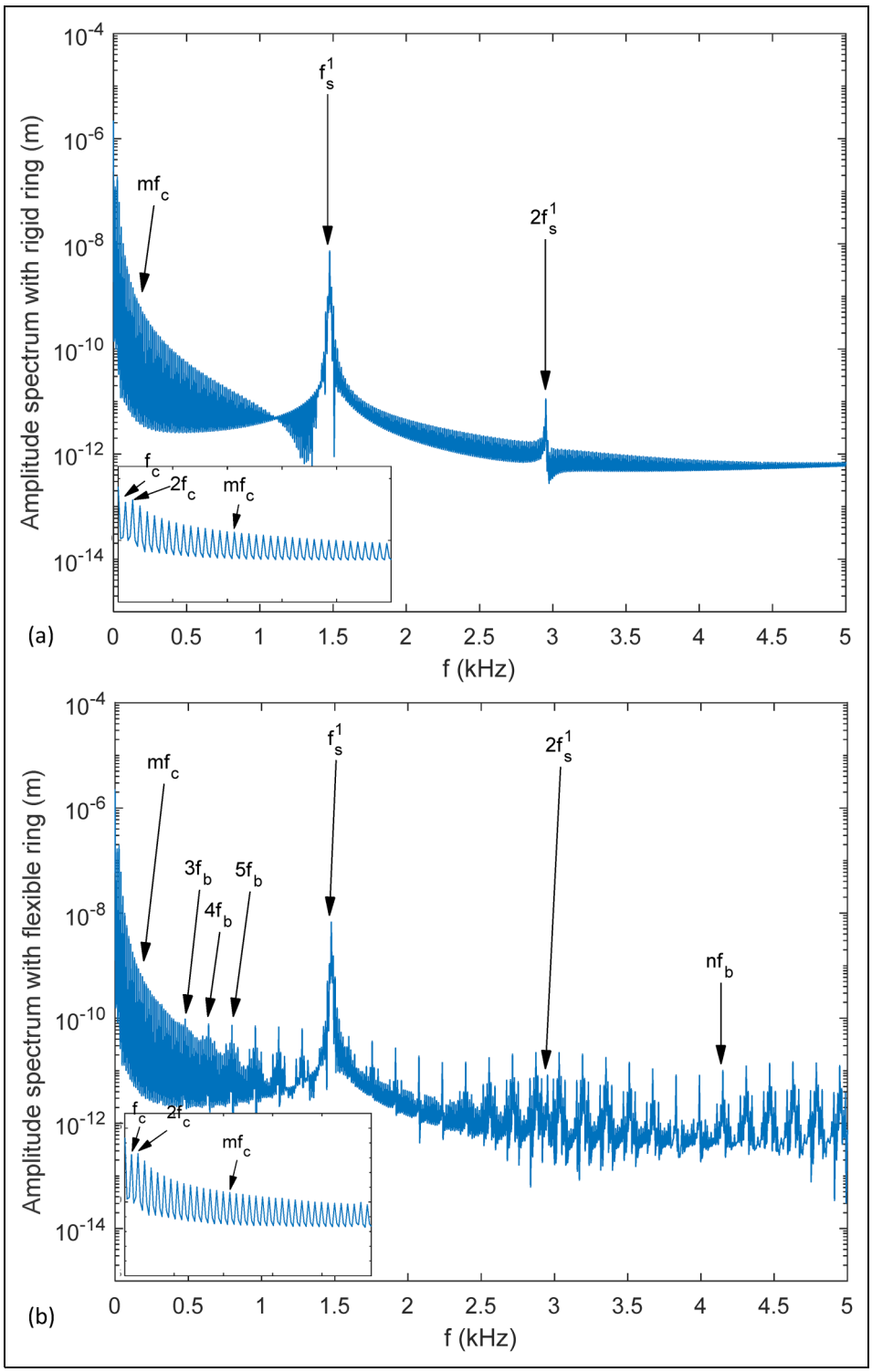

Figure 8. Spectrum of shaft vibrations in the band: 0–5 kHz and the zoomed-in views between 0 and 0.5 kHz: (a) rigid ring and (b) flexible ring.

lower x_e values due to the elastic deflection of the flexible ring. Hence, the stability points are somewhat shifted. The amplitudes of variations in velocity are slightly reduced for the case of a flexible outer bearing ring. Although the overall energy of the shaft has increased and its rigid motion is less stable, the modal vibrations due to shaft flexibility are slightly more stable than those for a rigid outer bearing ring. Clearly, as expected some energy is consumed in elastic deformation of flexible members which remains to accentuate vibrations in the case of assumed rigid members.

Time history and phase-displacement diagrams clearly show the large-scale displacement and stability behaviour of the rigid and flexible ring models. However, these are

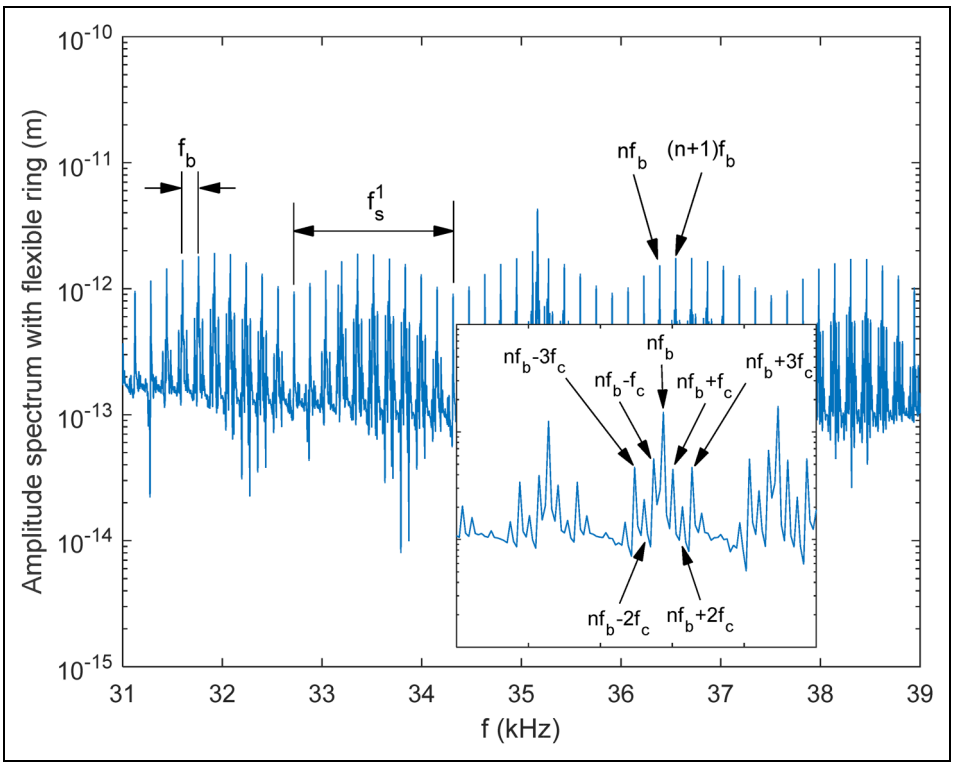

Figure 9. Influence of ring flexibility on amplification of higher orders of ball-pass frequency, nf_b, and its interactions with the first rigid mode of shaft, f_s^1.

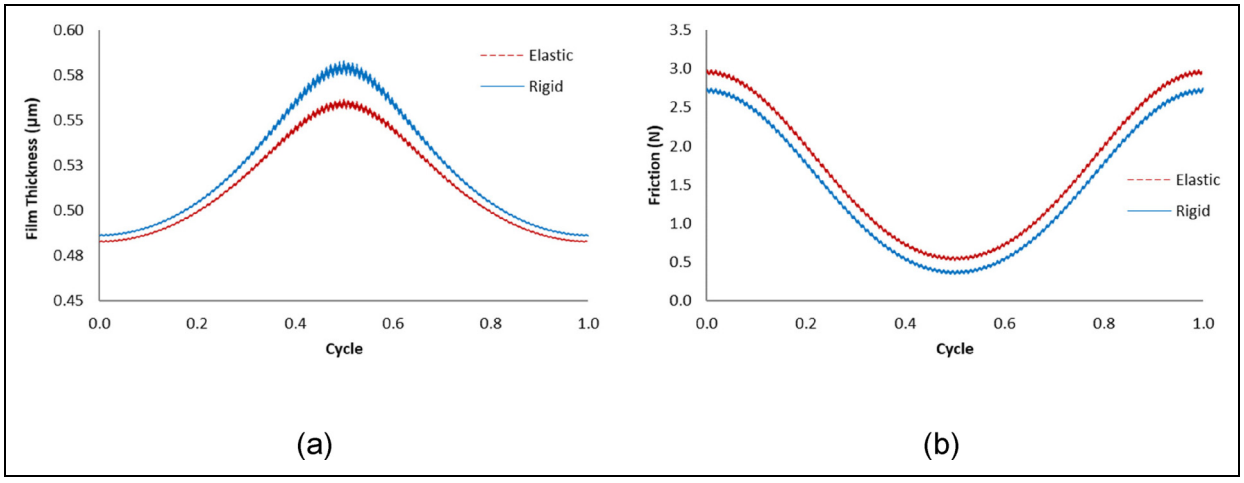

Figure 10. (a) Minimum film thickness and (b) friction for a ball in a single orbital motion.

insufficient to provide detailed differences between the responses of the two models. Hence, fast Fourier transformation is carried out. Spectra response of shaft vibrations are compared for the rigid ring and flexible ring models (Figure 7). The first five mode shapes of the elastic shaft are included in the simulations. The first mode represents the rigid mode of the shaft and modes 2–5 are related to its elastodynamic responses. The frequency content due to shaft modal vibrations is identical between the rigid and flexible ring responses. In both cases, the shaft modal frequencies are the main contributors to the spectra f_s^i, where $i = 1, 2, \ldots, 5$. The second and third significant contributors are the side-band responses at $f_s^i \pm f_s^1$ and $f_s^i \pm f_s^2$. These side-band frequencies show the interaction of higher shaft modal frequencies with the first (rigid) and second (first flexible) mode shapes. Side-band responses due to higher modal frequencies of the shaft are either infrequent or fairly negligible, for example, $2f_s^1$ and $f_s^5 - f_s^4$. These higher modal vibrations are largely masked by the shaft vibrations due to the presence of outer bearing ring flexibility (Figure 7(b)).

To better understand the root cause of the noise signatures in the flexible ring model, initially, the response spectra is investigated in the lower frequency range: 0–5 kHz (Figure 8). This frequency domain is selected

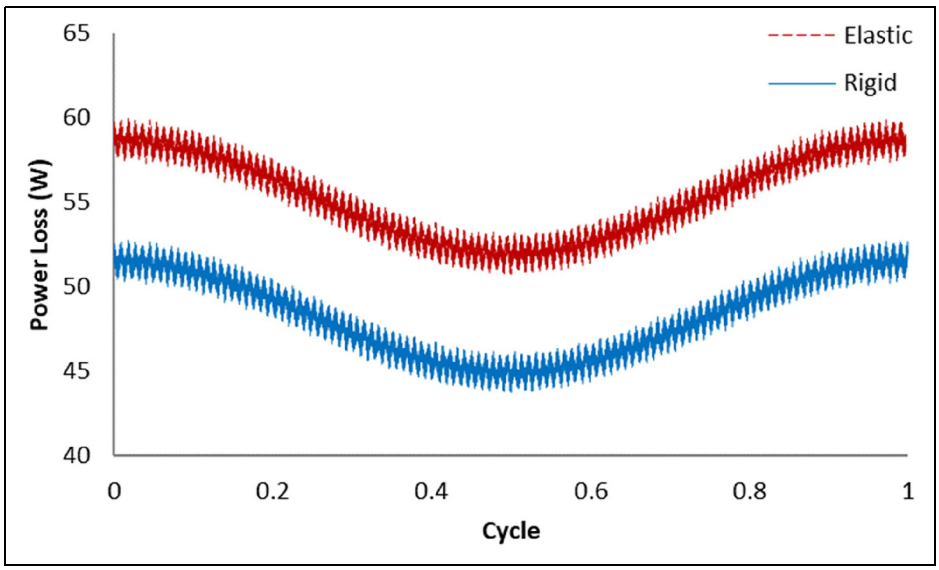

Figure 11. Predicted power loss.

because it only includes the first rigid mode of the shaft f_s^1 and its harmonic: $2f_s^1$. A zoomed-in window at the start of the vibrations is also provided to present a more detailed behaviour of the initial responses. In both models, the vibrations are initiated at the bearing cage response ($f_c = 13.3$ Hz):

$$f_c = \frac{f_{sh}}{2}\left(1 - \frac{d_b \cos\phi}{D_P}\right) = 13.3\ Hz \tag{38}$$

where f_{sh} is the shaft rotational frequency, ϕ is the contact angle. For a radial deep groove ball bearing $\phi = \pi / 2$.

The higher orders of cage response largely disappear at higher shaft vibration frequencies near 5 kHz. Another key bearing induced response is the ball-pass frequency ($f_b = 159.6$ Hz):

$$f_b = Zf_c = 159.6\ Hz \tag{39}$$

This spectral contribution is inherent in rolling element bearing response due to changes in the dynamic stiffness as the ball complement undergoes its orbital motion. This effect is termed variable compliance effect.[9,14,15,41,46] The modal responses of a flexible bearing ring exacerbate the variable compliance effect. These observed effects are similarly amplified across the low to high-frequency ranges (0–100 kHz) (Figures 7(b) and 8(b)). Figure 7(b) clearly shows contributions at multiples (harmonics) of the ball-pass frequency occurring regularly in the spectrum. To investigate these responses, a frequency range between 31 and 39 kHz is randomly selected (Figure 9). Additional frequency content clearly follows the multiples of the ball-pass frequency. These higher harmonics and their modulations with other spectral contents are always present in the rotor-bearing as shown in the acquired vibration spectra,[10,11,41,47–49] or in the various reported dynamic analyses.[14–16,21,25,35,50,51] The fluctuations in the amplitudes of these frequencies occur at the rigid body modal frequency of the shaft (f_s^1). The zoomed-in view of the n-th order of the ball-pass frequency suggests that additional vibrations can take place at the side-band frequencies related to the interactions with the multiples of the cage frequency.

Assessment of bearing performance

There have been very few lubricated bearing dynamics models[15,16,21,52,53] as this adds to the complexity of the analysis. However, incorporating lubricated contact dynamics into the analysis makes for realistic conditions, mimicking actual practice. In the current analysis, smooth rolling surfaces are assumed with sufficient radial interference so that the predominant regime of lubrication in the balls-races contacts remains elastohydrodynamic. With high loads and shear the lubricant can undergo non-Newtonian behaviour as described in section 2.1. Figure 10(a) shows the lubricant film thickness variation in a ball-race contact for a cage cycle for both cases of an assumed rigid as well as a flexible outer race. There is a reduction in the lubricant film thickness owing to the elastodynamics of the flexible bearing ring, constraining the gap in the contacts. Although the reduction in the film thickness is only very marginal, it increases the viscous contact friction as shown in Figure 10(b).

The overall effect of increased viscous friction is an increase in the overall frictional loss from the bearing as calculated using equation (24). This increased cyclic bearing frictional loss is shown in Figure 11. Friction is mainly generated by viscous shear of the lubricant and the sliding velocity of the balls to the races as the rolling elements roll and slide relative to the races due to the existence of a curvilinear ellipse in space.[41] The ring flexible elastodynamics influences the motions of the races and, therefore, the contact friction. There are many bearing cycles (cage rotations) in any application with 90–95% of all machines and mechanisms making use of rolling element bearings. Therefore, bearing losses occur as the result of elastodynamics of

bearing supports, which contribute to energy consumption and inefficiency of the machines worldwide.[54] It should be noted that rolling element bearing power losses are significantly lower than that of other forms of bearings and contacting pairs such as gears.

Concluding remarks

There has been a plethora of studies of rotor-bearing systems. These have included various important features, among many, in their analyses. However, very few studies have included the effect of rotor structural flexibility with lubricated contact dynamics including flexible outer race or housing. The current paper's main claim to originality resides in the integration of these practical aspects in rotor-bearing dynamics. The noted broad spectral response in vibration monitoring, not often presented in dynamic analysis, is obtained in much detail here. The combined investigation of shaft vibrations through time history, stability phase-displacement diagrams and FFT graphs clearly highlight the main shaft contributions and the secondary noise effects, originated from the ring flexibility on the nonlinear and transient vibrations of the flexible shaft. Ring flexibility has less impact in the shaft stability. However, it changes the location of the stability centres and spread of limit cycle vibrations. Moreover, ring flexibility amplifies the multiples of ball pass frequency even in the highest spectral region. These higher harmonics of ball pass frequencies induce cage responses in the form of side-band signatures, which would otherwise disappear at higher frequencies for the rigid ring model. Thus, including the elastodynamics of the rotor elements in the system vibration analyses would allow the identification of root causes of the noise and vibration in the system. Furthermore, it is shown that although the vibration signatures of such elements may not be clear in an acquired signal, their effect on the system energy efficiency can be quite significant. Therefore, shaft-bearing system vibration in its broad spectral response should be studied with the presence of lubricated contacts and frictional energy dissipation considerations. This detailed analysis shows that system dynamics and lubricated contact mechanics are closely intertwined and affect the overall system performance.

Acknowledgements

The authors gratefully acknowledge the financial support of the Engineering and Physical Sciences Research Council (EPSRC) extended to the Centre for Doctoral Training in Embedded Intelligence under the grant reference EP/L014998/1.

Declaration of conflicting interests

The authors declared no potential conflicts of interest with respect to the research, authorship, and/or publication of this article.

Funding

The authors disclosed receipt of the following financial support for the research, authorship, and/or publication of this article: This work was supported by the Engineering and Physical Sciences Research Council, (grant number EP/L014998/1).

ORCID iDs

Nader Dolatabadi https://orcid.org/0000-0003-3002-1665
Ramin Rahmani https://orcid.org/0000-0002-6084-8842

References

1. Kim SM and Lee SK. Prediction of thermo-elastic behavior in a spindle–bearing system considering bearing surroundings. *Int J Machine Tools and Manufacture* 2001; 41(6): 809–831.
2. Takabi J and Khonsari MM. On the thermally-induced failure of rolling element bearings. *Tribol Int* 2016; 94: 661–674.
3. Ma C, Zhao L, Shi H, et al. Experimental and simulation study on the thermal characteristics of the high-speed spindle system. *Proc IMechE, Part C: J Mech Eng Sci* 2017; 231(6): 1072–1093.
4. Lundberg G and Palmgren A. Dynamic capacity of rolling bearings. *J Applied Mech* 1949; 16: 165–172.
5. Ioannides E and Harris TA. A new fatigue life model for rolling bearings. *J Tribology* 1985; 107: 367–377.
6. Johns-Rahnejat PM and Gohar R. Point contact elastohydrodynamic pressure distribution and sub-surface stress field. In: Rahnejat H (ed.) *Proceedings of the tri-annual conference on multi-body dynamics: monitoring and simulation techniques*. Bradford, UK: Mechanical Engineering publications, 25–27 March 1997, pp. 161–179.
7. Harris TA. *Rolling bearing analysis*. Chichester, New York: John Wiley and Sons, 2001.
8. El Laithy M, Wang L, Harvey TJ, et al. Further understanding of rolling contact fatigue in rolling element bearings – a review. *Tribology Int* 2019; 140: 105849.
9. Wardle FP and Poon SY. Rolling bearing noise-cause and cure. *Chart Mech Eng* 1983; 30: 36–40.
10. Aini R, Rahnejat H and Gohar R. An experimental investigation into bearing-induced spindle vibration. *Proc IMechE, Part C: J Mech Eng Sci* 1995; 209: 107–114.
11. Vafaei S and Rahnejat H. Indicated repeatable runout with wavelet decomposition (IRR-WD) for effective determination of bearing-induced vibration. *J Sound and Vibration* 2003; 260: 67–82.
12. Abboud D, Elbadaoui M, Smith WA, et al. Advanced bearing diagnostics: a comparative study of two powerful approaches. *Mech Syst Signal Process* 2019; 114: 604–627.
13. Harris TA and Mindel MH. Rolling element bearing dynamics. *Wear* 1973; 23: 311–337.
14. Sunnersjö CS. Varying compliance vibrations of rolling bearings. *J Sound and Vibration* 1978; 58: 363–373.
15. Rahnejat H and Gohar R. The vibrations of radial ball bearings. *Proc IMechE, Part C: J Mech Eng Sci* 1985; 199: 181–193.
16. Aini R, Rahnejat H and Gohar R. A five degrees of freedom analysis of vibrations in precision spindles. *Int J Machine Tools and Manufacture* 1990; 30: 1–18.
17. Liu X and Yang P. On the thermal elastohydrodynamic lubrication of tilting roller pairs. *Tribology Int* 2013; 65: 346–353.
18. Kushwaha M, Rahnejat H and Gohar R. Aligned and misaligned contacts of rollers to races in elastohydrodynamic finite line conjunctions. *Proc IMechE, Part C: J Mechanical Engineering Science* 2002; 216: 1051–1070.

19. Ye Z, Wang L, Gu L, et al. Effects of tilted misalignment on loading characteristics of cylindrical roller bearings. *Mech Mach Theory* 2013; 69: 153–167.
20. Kushwaha M and Rahnejat H. Transient concentrated finite line roller-to-race contact under combined entraining, tilting and squeeze film motions. *J Physics, D: Applied Physics* 2004; 37: 2018–2034.
21. Mohammadpour M, Johns-Rahnejat PM and Rahnejat H. Roller bearing dynamics under transient thermal-mixed non-Newtonian elastohydrodynamic regime of lubrication. *Proc IMechE, Part K: J Multi-Body Dynamics* 2015; 229: 407–423.
22. Alfares M, Saleem O and Majeed M. Analytical study of thermal variation impact on dynamics of a spindle bearing system. *Proc IMechE, Part K: J Multi-Body Dynamics* 2019; 233: 871–898.
23. Gao Y, Li Z, Wang J, et al. Influences of bearing housing deflection on vibration performance of cylinder roller bearing–rotor system. *Proc IMechE, Part K: J Multi-Body Dynamics* 2013; 227: 106–114.
24. Cao L, Brouwer MD, Sadeghi F, et al. Effect of housing support on bearing dynamics. *J Tribology* 2016; 138: 011105.
25. Kerst S, Shyrokau B and Holweg E. A semi-analytical bearing model considering outer race flexibility for model based bearing load monitoring. *Mech Syst Signal Process* 2018; 104: 384–397.
26. Mao Y, Wang L and Zhang C. Influence of ring deformation on the dynamic characteristics of a roller bearing in clearance fit with housing. *Int J Mech Sci* 2018; 138: 122–130.
27. Turnbull R, Rahmani R and Rahnejat H. The effect of outer ring elastodynamics on vibration and power loss of radial ball bearings. *Proc IMechE, Part K: J Multi-Body Dynamics* 2020; 234: 707–722.
28. Matsubara M, Rahnejat H and Gohar R. Computational modelling of precision spindles supported by ball bearings. *Int J Machine Tools and Manufacture* 1988; 28: 429–442.
29. Sinou JJ, Villa C and Thouverez F. Experimental and numerical investigations of a flexible rotor on flexible bearing supports. *Int J Rotating Machinery* 2005; 3: 179–189.
30. Sinou JJ. Non-linear dynamics and contacts of an unbalanced flexible rotor supported on ball bearings. *Mech Mach Theory* 2009; 44: 1713–1732.
31. Liu J, Tang C and Pan G. Dynamic modeling and simulation of a flexible-rotor ball bearing system. *J Vib Control* 2022; 28: 3495–3509.
32. Chidamparam P and Leissa AW. Vibrations of planar curved beams, rings, and arches. *Appl Mech Rev* 1993; 46: 467–483.
33. Timoshenko SP. On the correction for shear of the differential equation for transverse vibrations of prismatic bars. *The London, Edinburgh, and Dublin Phil Magazine and J Science* 1921; 41(245): 744–746.
34. Rahnejat H, Rahmani R, Mohammadpour M and Johns-Rahnejat PM. Tribology of power train systems. *ASM Handb* 2017; 18: 916–934.
35. Rahnejat H. Computational modelling of problems in contact dynamics. *Eng Anal* 1985; 2: 192–197.
36. Whittemore HL and Petrenko SN. *Friction and carrying capacity of ball and roller bearings*. National Bureau of Standards, Technical Paper 201, Washington DC, 1921.
37. Hoffmann F and Rahnejat H. Constrained multi-body dynamic analysis of shaft and bearing systems, In Vibration and Control of Mechanical Systems, 2001: Presented at the 2001 ASME International Mechanical Engineering Congress and Exposition, November 11–16, 2001, New York.
38. Gohar R and Rahnejat H. *Fundamentals of tribology*. 3rd edition. London: World Scientific, 2018.
39. Hamrock BJ and Dowson D. Isothermal elastohydrodynamic lubrication of point contacts: part III—fully flooded results. *J Lubrication Technology* 1977; 99: 264–275.
40. Roelands CJA. "Correlational aspects of the viscosity-temperature-pressure relationship of lubricating oils, PhD Thesis, Delt University of Technology, 1966.
41. Lynagh N, Rahnejat H, Ebrahimi M, et al. Bearing induced vibration in precision high speed routing spindles. *Int J Machine Tools and Manufacture* 2000; 40: 561–577.
42. Eyring H. Viscosity, plasticity, and diffusion as examples of absolute reaction rates. *J Chemical Physics* 1936; 4: 283–291.
43. Briscoe BJ and Evans DCB. The shear properties of Langmuir–Blodgett layers. *Proc Roy Soc* 1982; 380: 389–407.
44. Polyanin AD. *Handbook of linear partial differential equations for engineers and scientists*. New York, NY: Chapman and Hall/CRC, 2001.
45. Rao SS. *Vibration of continuous systems*. New Jersey, NY: John Wiley & Sons, 2019.
46. Wardle FP. Vibration forces produced by waviness of the rolling surfaces of thrust loaded ball bearings part 1: theory. *Proc IMechE, Part C: J Mech Eng Sci* 1988; 202: 305–312.
47. Antoniadis I and Glossiotis G. Cyclostationary analysis of rolling-element bearing vibration signals. *J Sound and Vibration* 2001; 248: 829–845.
48. Vafaei S, Rahnejat H and Aini R. Vibration monitoring of high speed spindles using spectral analysis techniques. *Int J Machine Tools and Manufacture* 2002; 42: 1223–1234.
49. Guo W and Tse PW. A novel signal compression method based on optimal ensemble empirical mode decomposition for bearing vibration signals. *J Sound and Vibration* 2013; 332: 423–441.
50. Cong F, Chen J, Dong G, et al. Vibration model of rolling element bearings in a rotor-bearing system for fault diagnosis. *J Sound and Vibration* 2013; 332: 2081–2097.
51. Liu J, Xu Y and Shao Y. Dynamic modelling of a rotor-bearing-housing system including a localized fault. *Proc IMechE, Part K: J Multi-Body Dynamics* 2018; 232: 385–397.
52. Aini R, Rahnejat H and Gohar R. Vibration modeling of rotating spindles supported by lubricated bearings. *J Trib* 2002; 124: 158–165.
53. Chittenden RJ, Dowson D and Taylor CM. Power loss prediction in ball bearings. *In Tribology Series* 1989; 14: 277–286.
54. Bakolas V, Roedel P, Koch O, et al. A first approximation of the global energy consumption of ball bearings. *Tribol Trans* 2021; 64: 883–890.

Nomenclature

Roman symbols

A_o	cross-sectional area of outer elastic outer bearing ring
A_s	cross-sectional area of elastic shaft/rotor
a, b	contact footprint semi-major and semi-minor half-width
a_e	excitation acceleration

c shaft's constant
C radial clearance
D_p pitch circle diameter of the bearing
d_b ball diameter
E Young's modulus of elasticity
E' effective Young's modulus of elasticity of the contact
e curvature sum of the contacting profiles
F externally applied bearing forces
F_f friction
f_0 initial deflection of the shaft
$f_1,\ f_2$ reactions of support bearings 1 and 2
f_b ball-pass frequency
f_c cage rotational frequency
f_e excitation force per unit length of shaft
f_r applied radial force on the bearing outer race
f_{sh} shaft rotational frequency
f_s^i modal response frequencies of elastic shaft, $i = 1,\ 2,\ \ldots$ ($i = 1$: rigid mode)
G Green's function
G^* dimensionless materials' parameter
G_s shear modulus of elasticity
g_0 initial velocity of shaft
H_c^* dimensionless central contact lubricant film thickness
h lubricant film thickness
I second area moment of inertia
K effective contact stiffness for ball-to-races contacts
K_l combined contact stiffness at each raceway ($l = 1, 2$)
l length of shaft
$l_1,\ l_2$ position of support bearings 1 and 2
M shaft mass
m Harmonics of cage frequency
n Harmonics of ball-pass frequency
P total bearing power loss
p_0 maximum Hertzian contact pressure
p_c applied force in the circumferential direction of the bearing outer race
p_l instantaneous power loss
p_m mean contact pressure
R radius of curvature of surface profile
R_{io} inner radius of the outer bearing race
R_o radius of the outer race
t time
U speed of lubricant entraining motion
U^* dimensionless rolling viscosity parameter
u instantaneous radial global deflection of outer ring
u_e lateral deflection of shaft
u_s surface speed of inner race/rotor
W instantaneous contact load
W^* dimensionless load parameter
w instantaneous circumferential deflection of outer ring
x, y, z Cartesian coordinates
$x_e,\ y_e$ radial excursions of an elastic ring
$x_r,\ y_r$ radial excursions of a rigid ring
Z number of rolling elements
Z_0 lubricant piezo-viscosity index

Greek symbols

$\alpha,\ \beta$ transcendental functions of contact angle
α_p lubricant piezo-viscosity coefficient
δ localised Hertzian contact deflection
δ_d Dirac delta function
ε slope of lubricant limiting shear stress with pressure
ζ intermediate temporal variable
η effective lubricant viscosity
η_0 lubricant dynamic viscosity
θ instantaneous circumferential angular position
κ_c elastic proportionality constant
κ_s shear correction factor
λ ellipticity ratio of contact footprint
ν Poisson's ratio
ξ intermediate spatial variable
ρ density of shaft material
ρ_o density of bearing outer ring material
τ viscous shear stress
τ_0 characteristic shear stress
φ shaft/rotor modal shape function
ϕ contact angle
ψ auxiliary angle
ω response frequencies of flexible shaft

Abbreviations

DOF Degrees of Freedom
EHL Elastohydrodynamic Lubrication
FDM Finite Difference Method
FFT Fast Fourier transformation

Appendix

Discretisation of equations (32)-(34) provides the mass and stiffness matrices for the in-plane ring dynamic behaviour.

The in-plane inertial forces for a circumferential position i, representing instantaneous point of contact of the i-th ball take the form:

$$\begin{bmatrix} M_u & 0 & 0 \\ 0 & M_w & 0 \\ 0 & 0 & M_\phi \end{bmatrix} \begin{bmatrix} \ddot{u}_i \\ \ddot{w}_i \\ \ddot{\phi}_i \end{bmatrix} \tag{A1}$$

Hence, the mass matrix $[\ \boldsymbol{M}_{ip}\ ]$:

$$\boldsymbol{M}_{ip} = \begin{bmatrix} M_u & 0 & 0 \\ 0 & M_w & 0 \\ 0 & 0 & M_\phi \end{bmatrix} \tag{A2}$$

where the mass matrix constants are:

$$M_u = \rho A R \tag{A3}$$

$$M_w = \rho A R \tag{A4}$$

$$M_\phi = \rho I_2 R \tag{A5}$$

The in-plane elastic force for the same point i, takes the form:

$$\begin{bmatrix} K_{uu-1} & K_{uw-1} & K_{u\phi-1} & K_{uu} & K_{uw} & K_{u\phi} & K_{uu+1} & K_{uw+1} & K_{u\phi+1} \\ K_{wu-1} & K_{ww-1} & K_{w\phi-1} & K_{wu} & K_{ww} & K_{w\phi} & K_{wu+1} & K_{ww+1} & K_{w\phi+1} \\ K_{\phi u-1} & K_{\phi w-1} & K_{\phi\phi-1} & K_{\phi u} & K_{\phi w} & K_{\phi\phi} & K_{\phi u+1} & K_{\phi w+1} & K_{\phi\phi+1} \end{bmatrix} \begin{bmatrix} u_{i-1} \\ w_{i-1} \\ \phi_{i-1} \\ u_i \\ w_i \\ \phi_i \\ u_{i+1} \\ w_{i+1} \\ \phi_{i+1} \end{bmatrix} \tag{A6}$$

Hence, the stiffness matrix [$\boldsymbol{K}_{ip}$] becomes:

$$\boldsymbol{K}_{ip} = \begin{bmatrix} K_{uu-1} & K_{uw-1} & K_{u\phi-1} & K_{uu} & K_{uw} & K_{u\phi} & K_{uu+1} & K_{uw+1} & K_{u\phi+1} \\ K_{wu-1} & K_{ww-1} & K_{w\phi-1} & K_{wu} & K_{ww} & K_{w\phi} & K_{wu+1} & K_{ww+1} & K_{w\phi+1} \\ K_{\phi u-1} & K_{\phi w-1} & K_{\phi\phi-1} & K_{\phi u} & K_{\phi w} & K_{\phi\phi} & K_{\phi u+1} & K_{\phi w+1} & K_{\phi\phi+1} \end{bmatrix} \tag{A7}$$

where the stiffness matrix constants are:

$$K_{uu-1} = \frac{1}{\Delta\theta^2}\frac{\kappa AG}{R} \tag{A8}$$

$$K_{uw-1} = -\frac{1}{2\Delta\theta}\frac{\kappa AG}{R} - \frac{1}{2\Delta\theta}\frac{EA}{R} \tag{A9}$$

$$K_{u\phi-1} = \frac{1}{2\Delta\theta}\kappa AG \tag{A10}$$

$$K_{uu} = -\frac{2}{\Delta\theta^2}\frac{\kappa AG}{R} - \frac{EA}{R} \tag{A11}$$

$$K_{uw} = 0 \tag{A12}$$

$$K_{u\phi} = 0 \tag{A13}$$

$$K_{uu+1} = \frac{1}{\Delta\theta^2}\frac{\kappa AG}{R} \tag{A14}$$

$$K_{uw+1} = \frac{1}{2\Delta\theta}\frac{\kappa AG}{R} + \frac{1}{2\Delta\theta}\frac{EA}{R} \tag{A15}$$

$$K_{u\phi+1} = -\frac{1}{2\Delta\theta}\kappa AG \tag{A16}$$

$$K_{wu-1} = \frac{1}{2\Delta\theta}\frac{\kappa AG}{R} + \frac{1}{2\Delta\theta}\frac{EA}{R} \tag{A17}$$

$$K_{ww-1} = \frac{1}{\Delta\theta^2}\frac{EA}{R} \tag{A18}$$

$$K_{w\phi-1} = 0 \tag{A19}$$

$$K_{wu} = 0 \tag{A20}$$

$$K_{ww} = -\frac{2}{\Delta\theta^2}\frac{EA}{R} - \frac{\kappa AG}{R} \tag{A21}$$

$$K_{w\phi} = \kappa AG \tag{A22}$$

$$K_{wu+1} = -\frac{1}{2\Delta\theta}\frac{\kappa AG}{R} - \frac{1}{2\Delta\theta}\frac{EA}{R} \tag{A23}$$

$$K_{ww+1} = \frac{1}{\Delta\theta^2}\frac{EA}{R} \tag{A24}$$

$$K_{w\phi+1} = 0 \tag{A25}$$

$$K_{\phi u-1} = -\frac{1}{2\Delta\theta}\kappa AG \tag{A26}$$

$$K_{\phi w-1} = 0 \tag{A27}$$

$$K_{\phi\phi-1} = \frac{1}{\Delta\theta^2}\frac{EI_1}{R} \tag{A28}$$

$$K_{\phi u} = 0 \tag{A29}$$

$$K_{\phi w} = \kappa AG \tag{A30}$$

$$K_{\phi\phi} = -\frac{2}{\Delta\theta^2}\frac{EI_1}{R} - \kappa AGR \tag{31}$$

$$K_{\phi u+1} = \frac{1}{2\Delta\theta}\kappa AG \tag{A32}$$

$$K_{\phi w+1} = 0 \tag{A33}$$

$$K_{\phi\phi+1} = \frac{1}{\Delta\theta^2}\frac{EI_1}{R} \tag{A34}$$